MEASUREMENTS OF THE DIFFUSE ULTRAVIOLET BACKGROUND AND THE TERRESTRIAL AIRGLOW WITH THE SPACE TELESCOPE IMAGING SPECTROGRAPH[1]

THOMAS M. BROWN[2,4], RANDY A. KIMBLE[2,6], HENRY C. FERGUSON[3], JONATHAN P. GARDNER[2,7], NICHOLAS R. COLLINS[2,5,8], ROBERT S. HILL[2,5,9]

To appear in The Astronomical Journal

ABSTRACT

Far-UV observations in and near the Hubble Deep Fields demonstrate that the Space Telescope Imaging Spectrograph (STIS) can potentially obtain unique and precise measurements of the diffuse far-ultraviolet background. Although STIS is not the ideal instrument for such measurements, high-resolution images allow Galactic and extragalactic objects to be masked to very faint magnitudes, thus ensuring a measurement of the truly diffuse UV signal. The programs we have analyzed were not designed for this scientific purpose, but would be sufficient to obtain a very sensitive measurement if it were not for a weak but larger-than-expected signal from airglow in the STIS 1450–1900 Å bandpass. Our analysis shows that STIS far-UV crystal quartz observations taken near the limb during orbital day can detect a faint airglow signal, most likely from N I λ1493 Å, that is comparable to the dark rate and inseparable from the far-UV background. Discarding all but the night data from these datasets gives a diffuse far-ultraviolet background measurement of 501 ± 103 ph cm^{-2} sec^{-1} ster^{-1} Å^{-1}, along a line of sight with very low Galactic neutral hydrogen column ($N_{HI} = 1.5 \times 10^{20}$ cm^{-2}) and extinction ($E(B-V) = 0.01$ mag). This result is in good agreement with earlier measurements of the far-UV background, and should not include any significant contribution from airglow. We present our findings as a warning to other groups who may use the STIS far-UV camera to observe faint extended targets, and to demonstrate how this measurement may be properly obtained with STIS.

Subject headings: ultraviolet: general, atmospheric effects

1. INTRODUCTION

Over the past several decades, the far-ultraviolet background (FUVBG) has been the subject of many studies and the center of considerable controversy (for a review and an example of such debates, see Bowyer 1991; Henry 1991). The FUVBG is defined as the diffuse astronomical flux incident upon the Earth at wavelengths of 912–2000 Å, thus excluding sources such as terrestrial airglow and Galactic stars. Because the zodiacal light decreases dramatically below 2500 Å, and because the diffuse UV background is so faint, O'Connell (1987) has noted that this spectral region offers a window of very low sky background for observations of objects with faint surface brightness. We have been utilizing this spectral window for UV observations of faint extended sources, but these data also provide insight into the FUVBG itself.

A number of FUVBG measurements have shown a correlation between the FUVBG intensity and the Galactic neutral hydrogen column density (N_{HI}), leading to the conclusion that a significant fraction of the FUVBG must be Galactic in origin (see, e.g., the relatively recent data set of Hurwitz, Bowyer, & Martin 1991). In a 1400–1850 Å bandpass, extrapolating to $N_{HI} = 0$ gives an FUVBG intensity of $\sim$300 ph cm^{-2} sec^{-1} ster^{-1} Å^{-1}; this intensity increases to $\sim$1200 ph cm^{-2} sec^{-1} ster^{-1} Å^{-1} with increasing N_{HI}, but saturates before high column densities are reached (Hurwitz et al. 1991; Bowyer 1991). Curiously, measurements below Ly-α may indicate an upper limit of 30–100 ph cm^{-2} sec^{-1} ster^{-1} Å^{-1} (Henry 1991; Murthy et al. 1999), although this measurement has been contested (Edelstein, Bowyer, & Lampton 2000). Herein lies the controversy: a step in the FUVBG at Ly-α could imply an extragalactic origin for the $N_{HI} = 0$ component, such as redshifted Ly-α emission from an intergalactic medium (IGM) (Henry 1991); demonstration of such an origin of the FUVBG would have extremely important consequences, as canonical values for IGM parameters predict a negligible contribution to the FUVBG (e.g., Jakobsen 1993). On the other hand, others maintain that the dominant contribution to the $N_{HI} = 0$ component is mainly dust-scattered Galactic light (Bowyer 1991); under that assumption, the residual dust at $N_{HI} = 0$ that is needed to produce the FUVBG corresponds to $E(B-V) = 0.015$ mag (Hurwitz et al. 1991). We note that we cannot directly discriminate between an extragalactic and Galactic origin of the FUVBG, as we are measuring the FUVBG longward of Ly-α, but our measurements have all been taken along lines of sight with extremely low N_{HI} column *and* low dust extinction (see Table 1). New maps of Galactic extinction (Schlegel, Finkbeiner, & Davis 1998) are based on a direct measurement of the IR emission from the dust, instead of inferring the extinction from dust-to-hydrogen ratios; these new dust maps can potentially yield new insight into the FUVBG debate.

The Hubble Space Telescope (HST) currently employs one instrument with significant sensitivity in the far-UV: the Space Telescope Imaging Spectrograph (STIS) (Woodgate et al. 1998). However, STIS is not an ideal instrument for measuring the FUVBG: the throughput in the crystal quartz bandpass

[1]Based on observations with the NASA/ESA Hubble Space Telescope obtained at the Space Telescope Science Institute, which is operated by AURA, Inc., under NASA contract NAS 5-26555.

[2]Laboratory for Astronomy & Solar Physics, Code 681, Goddard Space Flight Center, Greenbelt, MD 20771
[3]STScI, 3700 San Martin Drive, Baltimore, MD 21218. ferguson@stsci.edu
[4]NOAO Research Associate. tbrown@pulsar.gsfc.nasa.gov
[5]Raytheon ITSS Corp.
[6]kimble@ccd.gsfc.nasa.gov
[7]gardner@harmony.gsfc.nasa.gov
[8]collins@zolo.gsfc.nasa.gov
[9]bhill@virgil.gsfc.nasa.gov

TABLE 1: Far-UV Data

Field ID	Exposure (sec)	RA (J2000)	Dec (J2000)	l (deg)	b (deg)	coverage (square arcsec)	N_{HI}[a] cm^{-2}	$E(B-V)$[b] (mag)
HDFN-Fol	124330	$12^h36^m44^s$	$+62^o12'12''$	125.908	+54.840	3659	1.51×10^{20}	0.01
HDFN-Par	17315	$12^h35^m41^s$	$+62^o10'38''$	126.124	+54.853	1003	1.51×10^{20}	0.01
HDFS-Pri	52124	$22^h33^m38^s$	$-60^o33'29''$	328.158	-49.274	878	2.39×10^{20}	0.03

[a] Dickey & Lockman (1990).
[b] Schlegel et al. (1998).

is not very high (peaking at 573 cm^2 effective area), the pixels and field of view are small (respectively 0.025″ and 25″), and the dark background is spatially and temporally variable (but very low). Nonetheless, we have found that the deepest imaging programs can yield interesting measurements of the diffuse UV background, because deep, high-resolution, coincident imaging at longer wavelengths can provide a mask for all objects brighter than $\sim$ 29 mag in the optical. Because we can mask very faint galaxies, we can determine how much of the FUVBG is truly diffuse. In this paper, we demonstrate the measurements of the FUVBG that could be made using the STIS far-UV camera. The programs we analyze here, from observations in and near the Hubble Deep Fields (HDFs), were not intended for measurements of the FUVBG, but they indicate that an HST program could be tailored to characterize the FUVBG with excellent statistics.

2. OBSERVATIONS

There are three programs with deep coincident far-UV and optical imaging that can potentially yield interesting measurements of the FUVBG: STIS followup imaging (General Observer Program 7410) of the HDF North (HDFN) (Williams et al. 1996), STIS parallel imaging (Guaranteed Time Observer Programs 7920 & 7921) during Near Infrared Camera and Multi Object Spectrometer (NICMOS) observations of the HDFN (Thompson et al. 1999), and primary STIS imaging (Gardner et al. 2000a) from the HDF South (HDFS) campaign (Williams et al. 2000). We will hereafter refer to each of these fields as HDFN-Fol, HDFN-Par, and HDFS-Pri. Each of these fields has optical imaging to a 3σ limiting AB mag of $\gtrsim$ 29. The far-UV data for these fields are summarized in Table 1. Note the N_{HI} and extinction along each line of sight are quite low; because the FUVBG intensity correlates with N_{HI}, we would expect measurements of the FUVBG to be near the minimum of $\sim$300 ph cm^{-2} sec^{-1} $ster^{-1}$ $Å^{-1}$ (Bowyer 1991; Hurwitz et al. 1991).

The UV imaging in each of these programs utilized the STIS far-UV camera with the crystal quartz filter (F25QTZ). This camera employs a multianode microchannel array (MAMA) instead of a charge-coupled device (CCD); there is no read noise, and very little sensitivity to cosmic rays. The minimum dark rate is 6.6×10^{-6} cts sec^{-1} pix^{-1}. The bandpass spans 1450–1900 Å, negating the signal from terrestrial Ly-α and O I λ1301 Å. Because the long wavelength cutoff of this bandpass is due to the rapidly dropping sensitivity of the detector's CsI photocathode, red leak is also negligible. A full description of the instrument can be found in Woodgate et al. (1998) and Kimble et al. (1998). The STIS photometric calibration is reliable at the 0.15 mag level, according to the STScI documentation (Baum et al. 1998).

Before our analysis, the lack of other known strong airglow lines in this bandpass at the HST altitude (600 km) implied that the airglow signal should be at least an order of magnitude below the minimum dark rate. Understandably, the spectral sky templates used for the STScI Exposure Time Calculator also make the same assumption. However, we have found that the sky signal can reach levels that are a significant fraction of the dark signal, if observations are made with HST near the limb during orbital day, as we discuss in §4.

Furthermore, the mean temperature of the far-UV camera has increased since STIS commissioning, and the dark background increases as a function of temperature. This increase appears as a "glow" that is strongest in the upper left-hand quadrant of the detector (Figure 1), where the dark rate can be 20 times higher than the minimum rate. Because the dark rate in this part of the detector is highly variable, we excluded this region during our analysis, thus rejecting over 75% of the available detector area. A cooler for the STIS camera should become available in Cycle 10, which would negate this problem and allow much more detector area for this measurement. A small portion of the detector is occulted by the aperture mask, appearing as a strip along the bottom $\sim$15 rows in STIS images; this region can be used to determine the dark rate in the exposed portions of the detector, away from the glow, as we discuss in §3.2.

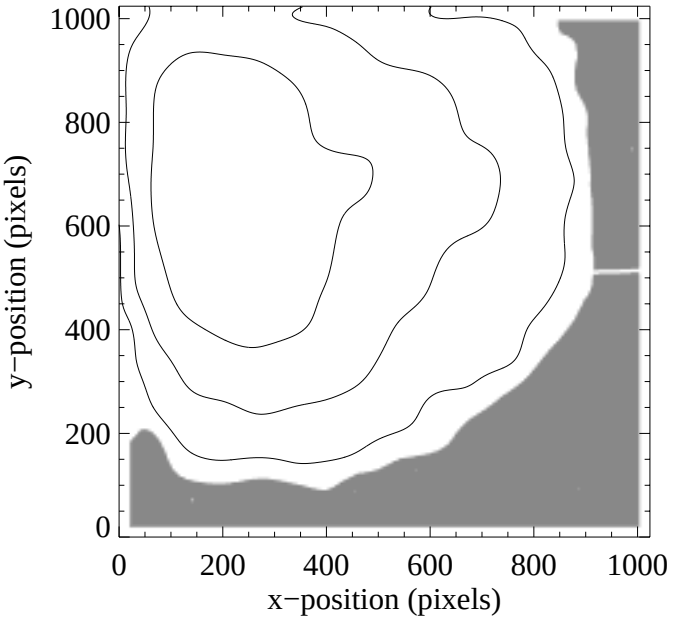

FIG. 1– A schematic of the STIS images used for measuring the FUVBG. When there is a strong dark background, its shape follows the contours shown (contour levels are at 2×, 5×, and 10× the lowest dark rate of 6.6×10^{-6} cts sec^{-1} pix^{-1}). The grey shading shows portions of the detector free from dark glow, hot pixels, edge effects, and repeller wire occultation; this portion of the detector is thus suitable for measuring the FUVBG.

2.1. *HDFN Followup Observations (HDFN-Fol)*

The original HDFN program produced observations of an undistinguished field at high Galactic latitude with the Wide Field Planetary Camera 2 (WFPC2), employing the F300W, F450W, F606W, and F814W filters (see Williams et al. 1996 for a complete description). A Cycle 7 General Observer Program (No. 7410) obtained observations of a portion of the field with the STIS far-UV and near-UV cameras. A total of 64 exposures spanning 124330 sec were obtained during a two year period (1997 December to 2000 February). The six STIS positions cover a roughly rectangular region of sky centered at RA(J2000)=$12^h36^m44^s$ and Dec(J2000)=$62^o12'12''$, with an area of 3659 square arcsec, and falling completely within the WF4 CCD HDFN image (which has an exposed area of 5926 square arcsec). Small dithers ($\sim$ 10 MAMA pixels) were employed between frames at each position, to smooth out small-scale changes in detector characteristics. Some of these STIS exposures were taken completely during orbital night, and all were taken near the limb (the zenith angle in these exposures ranged from 82–95^o). As we discuss in §4, the day exposures are contaminated by a faint sky signal that is inseparable from the FUVBG. The presumably uncontaminated night exposures were all taken in the two most northern positions, centered at RA(J2000)=$12^h36^m43^s$ and Dec(J2000)=$62^o12'34''$.

2.2. *NICMOS HDFN Parallel Observations (HDFN-Par)*

In 1998 January, Thompson et al. (1999) observed the original HDFN field with NICMOS, and STIS performed parallel imaging on a field $\sim 8.5'$ away. The exposure time for each frame was short, as a result of the parallel observing procedure. STIS observed in four imaging modes: far-UV (F25QTZ), near-UV (F25QTZ), clear CCD (50CCD), and long-pass CCD (F28X50LP), and one low-resolution near-UV spectroscopic mode (G230LB). The clear CCD and far-UV exposures each covered a roughly square region of sky, with respective areas of 3546 square arcsec and 1003 square arcsec, both centered at RA(J2000)=$12^h35^m41^s$ and Dec(J2000)=$62^o10'38''$. Dithers between far-UV frames ranged up to 200 MAMA pixels. The total exposure time was 34076 sec in the clear CCD mode and 17315 sec in the far-UV mode. Of the 45 far-UV frames, 30 exposures were taken completely in orbital night, for a total of 11500 sec; the remainder were taken completely in orbital day. Half of the night exposures spanned a zenith angle from 61–85^o, and half spanned a zenith angle from 33–48^o. The day exposures spanned a zenith angle from 47–69^o. The diffuse signal in the night exposures should have no contribution from airglow (see §5), but the day exposures clearly detected an airglow signal, although it was noticeably smaller than the day exposures from other programs that observed closer to the limb.

2.3. *STIS HDFS Primary Observations (HDFS-Pri)*

In 1998 October, STIS observed a field centered on a $z = 2.2$ quasar, using many imaging and spectroscopic modes, as part of the HDFS campaign (Williams et al. 2000). The imaging modes were the same as those used in the HDFN-Par observations and are described in Gardner et al. (2000a). The total exposure time was 155590 sec in the clear CCD mode, and 52124 sec in the far-UV mode. The far-UV and clear CCD exposures each covered a roughly square region of sky, with respective areas of 878 square arcsec and 3009 square arcsec, both centered at RA(J2000)=$22^h33^m38^s$ and Dec(J2000)=$-60^o33'29''$. Dithers between far-UV frames ranged up to 135 MAMA pixels. Unfortunately, none of the 25 far-UV exposures were taken completely during orbital night, and all observed far from the zenith (the zenith angle in these exposures ranges from 74–98^o). As we discuss in §4, all of these exposures were contaminated by faint airglow that is inseparable from the FUVBG.

3. DATA REDUCTION

Normally, multiple exposures of a field are registered and combined to produce a summed image. As we discuss below, we registered and summed our far-UV images to refine our knowledge of the offsets between the far-UV images, to verify the positional translation between the far-UV images and the optical images which would be used for object masking, and to allow a measurement of the far-UV flux originating in optically-detected objects. However, only a small portion of the detector is suitable for a measurement of the FUVBG; to measure the FUVBG, one must mask, for every exposure, the hot pixels, the pixels within the dark glow region (see Figure 1), and optically-detected objects. Although the dark glow can be subtracted (e.g., Gardner et al. 2000a; Brown et al. 2000), the residual noise in glow-subtracted regions is much higher than that in regions free of glow, and so a measurement of the FUVBG should avoid the detector region subject to glow. For these reasons, we found it simpler to measure the FUVBG in individual exposures, instead of a summed image; by examining the individual exposures, we were also able to check for sources of systematic errors, by looking for correlations between the measurements and observing conditions during a given exposure (e.g., day/night, limb angle, etc.).

3.1. *Creating Object Masks*

Before analyzing the far-UV images, we obtained the optical-band images that would be used to determine object masks. The version 1 HDFS images and the version 2 HDFN images are available from the STScI web site. The STIS CCD exposures of the HDFN-Par field were reduced by the standard reduction pipeline (including rejection of cosmic rays), registered and summed. On-chip 2×2 pixel binning produced a plate scale of $0.1''$ pix^{-1}. The plate scale for the STIS CCD image of the HDFS-Pri field is $0.025''$ pix^{-1} (via resampling of the dithered images), and for the WFPC2 images of the HDFN-Fol field it is $0.04''$ pix^{-1}. The variation in plate scale was unimportant for our purposes here, because we were merely using the optical images for object masking. Using the SExtractor package (Bertin & Arnouts 1996), an object catalog was made for each optical-band image. For the optical images of the HDFS-Pri and HDFN-Par fields, SExtractor was run on the summed clear CCD STIS images. For the optical image of the HDFN-Fol field, we made an object catalog from the combined WFPC2 F606W and F814W images. In each case, the 3σ limiting AB magnitude is $\gtrsim 29$.

We next performed a standard reduction and summation of the far-UV data. This process was already complete for the HDFS-Pri UV data (see Gardner et al. 2000a); we employed nearly identical methods for the HDFN-Fol and HDFN-Par UV data. In brief, the images were processed via the standard pipeline, excluding the dark subtraction, low-frequency flat field correction, and geometric correction. Dark frames from a six month period contemporaneous with each science frame were processed in the same manner, and those with a strong glow ($> 2 \times 10^{-5}$ cts sec^{-1} pix^{-1}) were summed and fit with a cubic spline to produce a glow profile appropriate for each frame (the shape of the glow changes slowly with time, and so

contemporaneous darks are required for this fit). A flat component and glow component to the dark background were then subtracted from each science frame, and then the flat field correction was applied. The frames were summed with the DRIZZLE package (Fruchter & Hook 1998), with registration, scaling, and geometric correction applied to give agreement with the optical image of each field. This summation was iterated several times to refine the relative offsets between individual far-UV frames. The pixels in each frame were weighted by EXPTIME^2/(SCALE^4 VARIANCE), where EXPTIME is the exposure time, SCALE is the ratio of the new pixel scale to the old pixel scale, and VARIANCE is the dark count variance. The weight map also included a hot pixel mask. Because the dark count variance is the product of the dark rate and the exposure time in a given pixel, our weight scales linearly with the ratio of the exposure time to the dark rate; equivalently, the exposures were weighted by the square of the signal-to-noise (S/N) ratio for sources that were fainter than the background, thus optimizing the summation to account for the temporal and spatial variations in the dark background. The statistical errors in each final drizzled far-UV image, for objects below the background, were given by the square root of the final drizzled weights map. In a separate paper (Gardner et al. 2000b), these registered images will also be used for an analysis of the far-UV number counts.

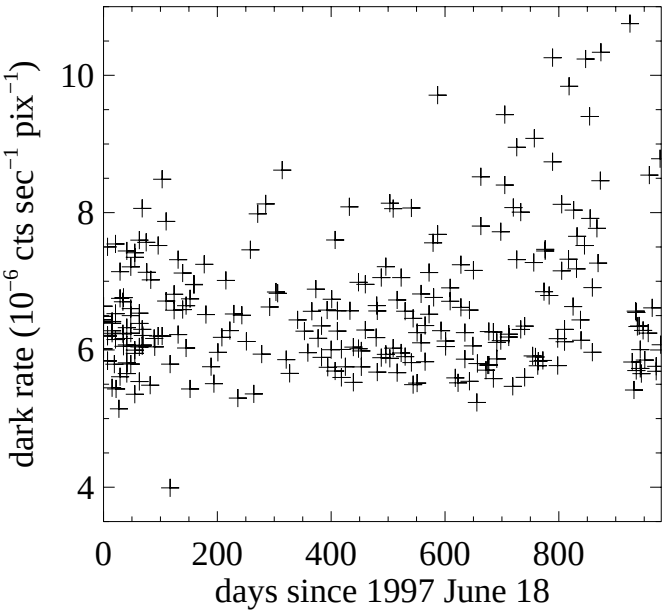

FIG. 2– These 268 dark exposures (1380 sec each) demonstrate the stability of the STIS dark rate in the region free of glow, hot pixels, and occulted pixels (see Figure 1). The mean dark rate for these exposures 6.6×10^{-6} cts sec^{-1} pix^{-1} with an rms of 1.0×10^{-6} cts sec^{-1} pix^{-1}. The late gap in the history is due to the safing of HST and subsequent servicing mission.

Once all of the far-UV frames were drizzled into a summed image for each of the three datasets, the BLOT package made it trivial to determine the object mask for each individual far-UV frame. Using BLOT (available with DRIZZLE as part of the IRAF DITHER package), the SExtractor segmentation map for each optical image was reverse-drizzled back to each individual far-UV frame, thus creating a tailored set of object masks for all of our far-UV frames. When combined with the detector mask shown in Figure 1, the remaining set of unmasked pixels in each exposure were suitable for measurements of the FUVBG. However, to measure the FUVBG, we first determined the dark rate in each frame.

3.2. *Dark Rate Determination*

As discussed in §2, the STIS far-UV camera has a very low but spatially and temporally variable dark rate that correlates with the detector temperature. At the time of this writing, there were 268 normal dark frames available in the STScI archive, 187 of which were taken during the time frame spanned by our science observations. The dark variation appears as a glow in the upper left hand quadrant of the detector (see Figure 1); when this glow is strong, it can peak at $20\times$ the low dark rate that exists outside of the glow. Pixels on the detector that are far from the glow have a much more stable dark rate (see Figure 2), of 6.6×10^{-6} cts sec^{-1} pix^{-1}, with an rms of 1.0×10^{-6} cts sec^{-1} pix^{-1} between dark frames.

To determine the dark rate in an individual frame, we took advantage of the fact that the aperture mask for the far-UV camera occults the bottom ~ 15 pixels in STIS images. By comparing the dark rate in rows 2–11 with the dark rate in that part of the detector appropriate for measuring the FUVBG (see Figure 1), we found that the occulted region consistently had a dark rate $1.1\times$ higher, due to edge effects with the microchannel plate signal processing. In our science frames, we assumed that the appropriately scaled rate in the occulted region gave the dark rate where we measured the FUVBG.

4. THE DIFFUSE FAR-UV BACKGROUND

For each far-UV exposure in all three datasets, we used IDL to calculate the net FUVBG signal in the unmasked portion of the detector. The mask included astronomical objects, hot pixels, occulted pixels, the dark glow region, and any pixel within 20 pixels of the image edge; the dark rate was determined from the occulted portion of the detector. We used the science frames that were reduced via the standard pipeline, excluding the dark subtraction, low-frequency flat field correction, and geometric correction; i.e., we did not include the later corrections explained in §3.1. Surprisingly, the FUVBG signal measured in each science frame varied much more than the expected variation from Poisson statistics (which included both the statistical uncertainty in the signal and the dark rate determination). The signal did not correlate with the strength of the dark glow, thus ruling out an incomplete masking of the glow region. Instead, the signal correlated with the fraction of the observation taken during orbital day, as shown in Figure 3.

The HDFS-Pri and HDFN-Fol UV data were all taken near the limb (as opposed to HDFN-Par UV data - see §2.2). These two near-limb datasets, taken together, show a strong correlation between our attempted FUVBG measurement and that fraction of the exposure spent in orbital day: the Pearson's linear correlation coefficient is 0.77. Fitting a line to these points and errors gave a y-intercept of 379 ± 57 ph cm^{-2} sec^{-1} ster^{-1} Å^{-1} for near-limb observations at complete orbital night. However, the variation in the airglow was clearly affected by more parameters than the "day fraction" of the exposure, because the points taken in complete orbital day show a large degree of variation: the rms of the points in complete orbital day is 576 ph cm^{-2} sec^{-1} ster^{-1} Å^{-1}, while the statistical errors are half that size. Much of this variation is likely due to the variations in limb angle. Thus, the linear fit shown in Figure 3 is simply a rough approximation of the trend in these data. The HDFN-

Par UV observations are not included in Figure 3, because they were all taken in either complete orbital day or night with very short exposure times, and thus large statistical uncertainties.

Two of the programs discussed herein include data taken in complete orbital night: the HDFN-Fol and the HDFN-Par programs. For those night exposures, we calculated a weighted sum of the diffuse dark-subtracted signal in each frame, where the weight is the product of the number of exposed pixels and the exposure time, thus maximizing the S/N and minimizing the contribution from brief exposures with few unmasked pixels. The measurement from the night HDFN-Par frames is 296 ± 135 ph cm^{-2} sec^{-1} ster^{-1} Å^{-1}, and the measurement from the night HDFN-Fol frames is 712 ± 157 ph cm^{-2} sec^{-1} ster^{-1} Å^{-1}; together, the entire set of night frames yields a measurement of 501 ± 103 ph cm^{-2} sec^{-1} ster^{-1} Å^{-1}. As shown in Table 1, both of these fields sample Galactic sight-lines with very low N_{HI} and extinction (the excluded dayglow-contaminated HDFS-Pri data samples a sight-line with somewhat higher hydrogen column and extinction). Our night measurement of the FUVBG is in good agreement with the earlier measurements of 300 ph cm^{-2} sec^{-1} ster^{-1} Å^{-1}, calculated by extrapolating to $N_{HI} = 0$ (Bowyer 1991 and references therein). Although we could not determine from these data alone if there was a contribution from airglow in our night measurement, many experiments have shown that the night airglow should be several orders of magnitude below the STIS dark rate. We discuss possible contamination from airglow in the next section.

5. AIRGLOW

The STIS crystal quartz filter blocks emission shortward of 1450 Å very effectively, and the long wavelength cutoff of the far-UV bandpass is due to detector sensitivity; the varying signal detected in our near-limb day observations probably originated in airglow within the 1450–1900 Å bandpass. The strongest airglow line in this wavelength range is N I λ1493 Å (Eastes et al. 1985; Budzien, Feldman, & Conway 1994). Viewing at an altitude of $\sim$ 200 km and 90^o to the zenith (in 1980, near the solar maximum) Eastes et al. (1985) observed $\sim$ 1000 R of N I dayglow emission. For atomic nitrogen at an altitude of 200–600 km, the scale height is $kT/(Mg) \approx 60$ km. STIS observes at an altitude of 600 km, and the observations described herein were also all taken within a few years of solar maximum; at 6.7 scale heights above the measurements of Eastes et al. (1985), STIS might expect to observe about one rayleigh of N I, which translates to 6×10^{-7} cts sec^{-1} pix^{-1}. Instead, from Figure 3, we see that exposures in complete orbital day produced a net dark-subtracted signal that was 2–8 times higher. Thus, the STIS signal may reflect the combined contribution from several weaker sky emission lines, and/or the fact that the optically-thin N I emission is not accurately described by the approximation we have used here.

Eastes et al. (1985) showed that there are several N_2 Lyman-Birge-Hopfield (LBH) emission lines in the 1450–1900 Å bandpass. These lines are individually somewhat weaker than the N I emission, but their summed signal is several thousand rayleigh at an altitude of 200 km. However, the scale height of N_2 is only 30 km, so the contribution from the LBH emission should be negligible at 600 km.

Observing near solar maximum from the Space Shuttle at an altitude of 358 km, Waller et al. (1995) also found significant dayglow emission in a bandpass similar to the STIS far-UV bandpass; they attributed their 150 R of near-limb emission to both N I and N_2. At 2.6 N I scale heights and 5.3 N_2 scale heights above the Eastes et al. (1985) measurements, one would expect 75 R of N I emission and $\sim$10 R of N_2 emission. Thus, Waller et al. (1995) observed about twice as much near-limb dayglow as one might expect from extrapolating the measurements of Eastes et al. (1985), and the far-UV dayglow measurements at 200 km, 358 km, and 600 km all agree within an order of magnitude.

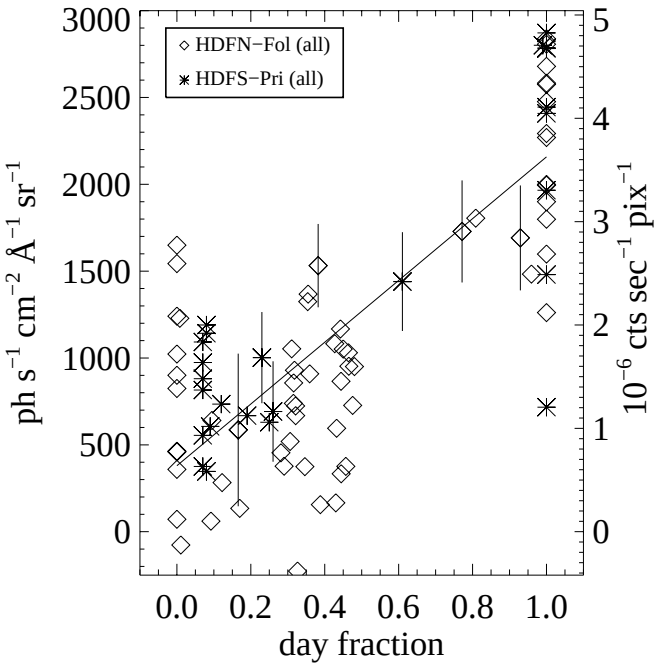

FIG. 3– Our measurements of the FUVBG from exposures near the limb, versus that fraction of the exposure taken during orbital day. Measurements from the HDFN-Fol UV data (*diamonds*) and the HDFS-Pri UV data (*asterisks*) are shown with a representative sample of their statistical uncertainties. The variation among these measurements is larger than that expected from the statistics, and correlates with the fraction of the exposure taken in orbital day. The line shows the uncertainty-weighted fit to these data, with a y-intercept of 373 ± 67. For data taken in complete orbital night, there should be no signal from airglow (see §5). Note that the net diffuse signal that we measured was always less than the STIS dark rate (compare the right-hand y-axis with Figure 2), but it was a nonnegligible contribution to the total background in near-limb day observations.

Previous observations of far-UV airglow during orbital night showed signals that were far below those observed during the day. For example, observing near the limb at an altitude of 330 km, Morrison et al. (1992) easily detected a few tenths of a rayleigh in O I emission lines at 1301 and 1356 Å, but did not detect the much weaker N I 1493 Å emission, nor any other line that would produce significant airglow in the STIS bandpass. Morrison et al. (1992) observed near solar minimum, while STIS observed near solar maximum, but the STIS night observations were taken at an altitude that is 4 scale heights above the measurements of Morrison et al. (1992); the STIS observations should be completely insensitive to N I airglow, for any zenith angle $< 95^o$ (at an HST altitude of 600 km, a sight line along a zenith angle of 95^o only intersects atmospheric heights $>$ 575 km). However, it is troubling that the HDFN-Fol measurement of the FUVBG (taken over a zenith angle of 82–95^o) is considerably higher than the HDFN-Par measurement (taken

at in two zenith angle ranges of 61–85° and 33–48°). We show the individual night measurements of the FUVBG versus limb angle in Figure 4. The statistics are poor, but there is a slight trend for an increasing signal as one moves to higher limb angle; the Pearson's linear correlation coefficient for the signal versus zenith angle, for the points above a zenith angle of 60°, is 0.33 (it is only 0.13 if the points at all zenith angles are included, but the nonlinear increase in signal should mainly occur as one approaches the limb). We stress that experiments at lower altitudes indicate that our night FUVBG measurements should have no significant contribution from airglow. A well-designed STIS measurement of the FUVBG should be taken in TIMETAG mode, which would allow the extraction of night-only data from long exposures, and demonstrate the sensitivity (or lack thereof) to zenith angle.

6. EMISSION FROM RESOLVED OBJECTS

Because our object masks were derived from very deep optical images, we masked all objects to an optical AB magnitude of 29 in our far-UV images, giving a measure of the truly diffuse far-UV emission. In a subsequent paper, we will discuss in detail the far-UV emission from these objects, but it is worth noting here their summed contribution to these fields. For this measurement, we used the drizzled sum of far-UV exposures in each field (see §3.1), including those regions affected by the dark glow. A glow profile was subtracted from the individual frames before drizzling, and any residual dark glow was subtracted as part of the local sky value for each object. The increased noise in the regions of higher dark rate does not significantly reduce the S/N ratio of this measurement. Instead, the dominant source of error is the incomplete sampling of the number counts, due to the small sky coverage.

To determine the flux for each object, we summed the countrate within the area for each object, using the SExtractor segmentation map to define that area, and then subtracted the mean local background within a $6'' \times 6''$ box. Our method was the same as that used for the HDFS catalog (Gardner et al. 2000a), which includes a detailed description of the procedure. In the HDFN-Par UV data, the emission originating in optically-detected objects is 94 ± 14 ph cm^{-2} sec^{-1} ster^{-1} Å^{-1}. In the HDFN-Fol UV data, we measured 60 ± 4 ph cm^{-2} sec^{-1} ster^{-1} Å^{-1} in optically-detected objects, although the measurement drops to 45 ± 4 ph cm^{-2} sec^{-1} ster^{-1} Å^{-1} if one excludes a blue Galactic star from the field. In the HDFS-Pri data, we measured 26 ± 5 ph cm^{-2} sec^{-1} ster^{-1} Å^{-1} in optically-detected objects, excluding the very bright target $z = 2.2$ quasar in the center of the field. The uncertainty in these measurements was dominated by the inadequate sampling of the UV number counts, which exceeded the errors quoted here for photon counting statistics. The contribution from faint objects in these fields shows that galaxies will make a nonnegligible (though not dominant) contribution to a measurement of the FUVBG if they are not properly masked or subtracted via an assumed UV number counts distribution.

7. DISCUSSION

Restricting our data to that obtained in orbital night, we measured a diffuse far-UV background of 501 ± 103 ph cm^{-2} sec^{-1} ster^{-1} Å^{-1}. Our 5σ detection of the FUVBG, a signal that is $\sim$10% of the STIS dark rate, is in reasonable agreement with earlier measurements at low N_{HI}. However, the unique aspect to STIS measurements of the FUVBG is that STIS can measure a truly diffuse signal, because high-resolution coincident imaging in the far-UV and optical bandpasses allows masking of all objects down to a very faint magnitude.

The night data used for our measurement of the FUVBG were taken in two fields at high Galactic latitude, separated by about 8.5 arcmin. The measurement in the HDFN-Par field was 296 ± 135 ph cm^{-2} sec^{-1} ster^{-1} Å^{-1}, and the measurement in the HDFN-Fol field was 712 ± 157 ph cm^{-2} sec^{-1} ster^{-1} Å^{-1}. The HDFN-Fol field was observed much closer to the Earth's limb than the HDFN-Par field, but the night exposures should show no measurable contribution from airglow. Barring systematic errors, the difference between the two fields may reflect a true patchiness in the FUVBG, whether it originates in scattering from Galactic dust or an extragalactic source. Note that the Galactic $E(B-V)$ along each line of sight is very low (0.01 mag).

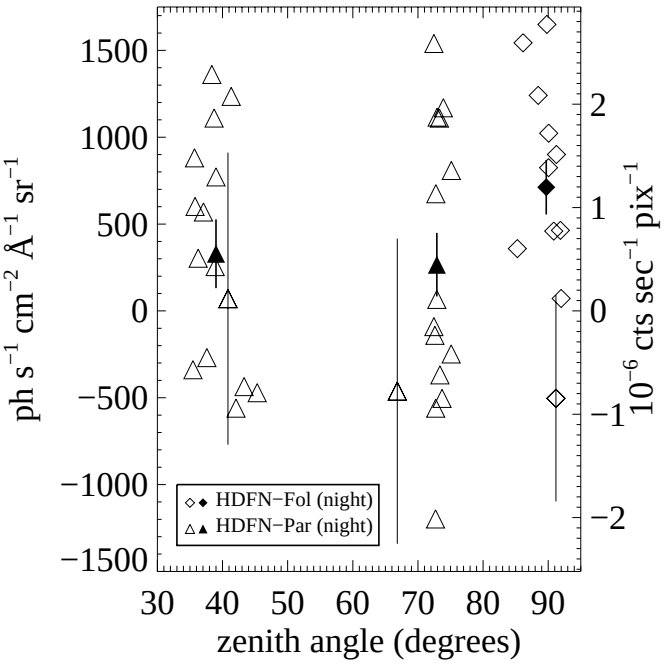

FIG. 4– Our measurements of the FUVBG, as a function of the average zenith angle during the exposure, using only those exposures taken in complete orbital night. Individual measurements from the HDFN-Fol data (*open diamonds*) and the HDFN-Par data (*open triangles*) are shown with a representative sample of their associated uncertainties. The filled symbols show the sum of the measurements near 39°, 73°, and 90°, with their associated uncertainties; there is a weak trend for increasing signal at high zenith angle (near the limb, which is at 114°), but the known night airglow in this bandpass should be completely negligible at the HST altitude of 600 km. The sum of the data taken at a zenith angle less than 80° is 296 ± 135 ph cm^{-2} sec^{-1} ster^{-1} Å^{-1}, and the sum of the data taken at a zenith angle greater than 80° is 712 ± 157 ph cm^{-2} sec^{-1} ster^{-1} Å^{-1}.

To measure the FUVBG with high statistical certainty, future STIS observations should be obtained in TIMETAG mode, to exclude day data, and to ensure that the night data shows no correlation with zenith angle. The target should be a reasonably empty portion of a field with deep optical imaging, such as one of the fields described herein. If the STIS cooling system to be installed in HST Servicing Mission 3B is as effective as expected in eliminating dark glow, a much larger fraction of the detector area will be available for sensitive measurements. Off-nominal positioning of the entrance aperture mask could also

increase the shadowed detector area available for concurrent monitoring of the dark rate, though HST operating constraints may not permit this.

Prior to our analysis, the crystal quartz filter on the STIS far-UV camera was thought to produce a bandpass that was completely insensitive to both zodiacal emission and airglow. Because the dark rate in this camera is so low, the low sky enables photometric measurements of very faint extended UV sources (see, e.g., Brown et al. 2000). However, our analysis showed that while the sky signal is always lower than the dark rate, it may be nonnegligible. The dark glow can increase the background signal by a factor of 20 in sections of the detector, but the sky can reach levels comparable to the minimum dark rate; the sky can thus increase the background signal by a factor of two in the darkest parts of the detector during near-limb day observations. Potential STIS observers should take this sky signal into account when planning their S/N estimates, if they will be observing near the limb (e.g., in the HST Continuous View Zone).

Support for this work was provided by NASA through the STIS GTO team funding. TMB acknowledges support at GSFC by NAS 5-6499D. We are grateful to P. D. Feldman for discussions of UV airglow. We are grateful to R. Thompson for allowing parallel STIS observations to the NICMOS HDF imaging program.

REFERENCES

Baum, S., et al. 1998, Space Telescope Imaging Spectrograph Instrument Handbook, (Baltimore: STScI), 315
Bertin, E., & Arnouts, S. 1996, A&AS, 117, 393
Bowyer, S. 1991, ARAA, 29, 59
Brown, T. M., Bowers, C. W., Kimble. R. A., & Ferguson, H. C. 2000, ApJ, 529, L89.
Budzien, S. A., Feldman, P. D., & Conway, R. R. 1994, JGR, 99, 23275
Dickey, J. M., & Lockman, F. J. 1990, ARA&A, 28, 215
Eastes, R. W., Feldman, P. D., Gentieu, E. P., & Christensen, A. B. 1985, JGR, 90, 6594
Edelstein, J., Bowyer, S., & Lampton, M. 2000, ApJ, in press
Fruchter, A. S., & Hook, R. N. 1998, PASP, submitted, astro-ph/9808087
Gardner, J. P., et al. 2000a, AJ, 119, 486
Gardner, J. P., et al. 2000b, in prep.
Henry, R. C. 1991, ARAA, 29, 89
Hurwitz, M., Bowyer, S., & Martin, C. 1991, ApJ, 372, 167
Jakobsen, P. 1993, in Extragalactic background radiation : a meeting in honor of Riccardo Giacconi : proceedings of the Extragalactic Background Radiation Meeting, ed. D. Calzetti, M. Livio, & P. Madau (New York: Cambridge University Press), 75
Kimble, R. A., et al. 1998, ApJ, 492, L83
Morrison, D., Feldman, P. D., & Henry, R. C. 1992, JGR, 97, 1633
Murthy, J., Hall, Earl, M., Henry, R. C., & Holberg, J. B. 1999, ApJ, 522, 904
O'Connell, R. W. 1987, AJ, 94, 876
Schlegel, D. J., Finkbeiner, D. P., & Davis, M. 1998, ApJ, 500, 525
Thompson, R. I., Storrie-Lombardi, L. J., Weymann, R. J., Rieke, M. J., Schneider, G., Stobie, E., & Dyer, L. 1999, AJ, 117, 17
Waller, W. H., et al. 1995, AJ, 110, 1255
Williams, R. E., et al. 2000, in prep
Williams, R. E., et al. 1996, AJ, 112, 1335
Woodgate, B. E., et al. 1998, PASP, 110, 1183